Article

One-Step Electrospun LTO Anode for Flexible Li-Ion Batteries

Edi Edna Mados [1,2,3], Roni Amit [4], Noy Kluska [4], Diana Golodnitsky [1,*] and Amit Sitt [1,2,3,*]

1   School of Chemistry, Faculty of Exact Sciences, Tel Aviv University, Tel Aviv 69978, Israel
2   Jan Koum Center for Nanoscience and Nanotechnology, Tel Aviv University, Tel Aviv 6997801, Israel
3   The Center for Physics & Chemistry of Living Systems, Tel Aviv University, Tel Aviv 6997801, Israel
4   Department of Materials Science and Engineering, Tel Aviv University, Tel-Aviv 69978, Israel
*   Correspondence: golod@tauex.tau.ac.il (D.G.); amitsitt@tauex.tau.ac.il (A.S.)

Abstract

Fiber-based and fabric batteries signify a groundbreaking development in energy storage, allowing for the straightforward incorporation of power sources into wearable fabrics, intelligent apparel, and adaptable electronics. In this study, we introduce a novel strategy for one-step fabrication of a flexible lithium titanate oxide ($Li_4Ti_5O_{12}$, LTO) anode directly on a copper current collector via electrospinning, eliminating the need for high-temperature post-processing. Based on our previous work with electrospun nanofiber cathodes and carbon-based current collector, we prepared the LTO electrode using polyethylene oxide (PEO) as a binder and carbon additives to enhance mechanical integrity and conductivity. LTO fiber mats detached from the current collector were found to endure multiple instances of bending, twisting, and folding without any structural damage. LTO/Li cells incorporating electrospun fiber LTO electrodes with 72 wt% active material loading deliver a high capacity of 170 mAh g^{-1} at 0.05 C. In addition, they demonstrate excellent cycling stability with a capacity loss of only 0.01% per cycle over 200 cycles and maintain a capacity of 160 mAh g^{-1} at 0.1 C. The scalability of the heat-treatment-free method for fabricating flexible LTO anodes, together with the improved mechanical durability and electrochemical performance, offers a promising route toward the development of next-generation flexible and wearable energy storage devices.

Keywords: flexible Li-ion batteries; LTO Anode; electrospinning; fabric batteries; wearable energy storage

1. Introduction

Lithium-ion batteries (LIBs) have emerged as the leading energy storage solution over the past few decades, owing to their superior energy and power density [1,2]. With the increasing demand for compact, flexible, and mechanically robust micro-batteries, advanced electrode materials that can sustain high electrochemical performance while meeting the structural requirements of next-generation flexible and wearable energy storage systems are needed [3,4].

Recent research efforts have been strongly centered on developing flexible anodes for such applications. Various strategies that have yielded promising results in terms of capacity and cycling stability include the integration of binder-free composites such as Co_9S_8/rGO supported on a carbon cloth [5], graphene/Mn_3O_4 nanocomposite membrane [6], and conductive CNT-cellulose aerogels coated with Si via plasma-enhanced chemical vapor deposition [7]. While these systems show considerable potential, the majority require multi-step fabrication or post-processing under harsh conditions, such as

high-temperature annealing or chemical vapor deposition, which hinder scalability and often compromise flexibility [8].

In our previous study, we demonstrated the feasibility of polymer-based LiFePO$_4$ (LFP) cathode/current-collector micro-meshes with bi- and interlayered architectures fabricated via electrospinning, highlighting the method's capability to produce flexible, mechanically resilient, and conductive electrodes suitable for integrated energy storage devices [9]. Building upon these findings, the present work extends this strategy to the anode side by developing flexible Li$_4$Ti$_5$O$_{12}$ (LTO) fibers through a one-step electrospinning process.

Among various anode materials, "zero-strain" Li$_4$Ti$_5$O$_{12}$ has attracted significant attention owing to its excellent safety, stable operating voltage (1.55 V vs. Li/Li$^+$), which lies within the stability window of common electrolytes [10,11], and negligible volume change during cycling (~0.1%) [12–14]. These features suppress lithium dendrite growth and reduce the formation of an unstable solid-electrolyte interphase (SEI) layer, a common issue in graphite-based anodes [15,16]. Despite these advantages, the widespread practical application of LTO is hindered by its inherent kinetic limitations, including intrinsically low electronic conductivity and poor Li-ion diffusion ability. Spinel LTO is considered an insulator in its pristine state, due to the electronic configuration of Ti^{+4} [14,17]. While lithiation of Li$_7$Ti$_5$O$_{12}$ can increase electronic conductivity significantly and mixed-valence states of Ti^{+3}/Ti^{+4} at phase interfaces can enhance electron migration, the material still faces challenges in high-rate capability [14,17,18].

To address these limitations, 3D porous architectures and nanostructured LTO morphologies have been explored, because they enable enhanced ion transport, better electrolyte accessibility, and improved electrode kinetics [19–22]. Electrospinning has emerged as a versatile method to produce such architectures with fibrous, interconnected networks that offer both high surface area and mechanical flexibility [17]. Yet, in conventional electrospun LTO systems reported to date, high-temperature post-treatments (typically >600 °C) are routinely employed to decompose polymer carrier or crystallize LTO precursors to form the spinel phase [23–28]. These steps cause thermal shrinkage, fiber embrittlement, partial loss of active material or conductive additives, and demand complex thermal infrastructure, all of which undermine the potential for flexible device integration. A detailed comparison of electrospun anodes reported in the literature is provided in the Supplementary Materials (S1) [23–32].

In this study, we report a novel one-step electrospinning process for fabricating flexible LTO anode fibers that eliminates the need for post-thermal treatment. This approach preserves the as-spun fiber networks' mechanical integrity, avoiding cracking and delamination associated with high temperature processing. To the best of our knowledge, this is the first demonstration of thermally untreated electrospun LTO mats with structural cohesion suitable for integration in flexible energy storage systems. Electrochemical measurements imply that these electrodes deliver capacities close to the theoretical value at low discharge rates, demonstrating their potential for stable low-power applications. At higher current densities, capacity limitations arise from diffusion-related constraints, revealing the trade-off between mechanical robustness and high-rate performance. Our method offers a scalable, energy-efficient pathway to flexible LTO anodes and highlights the design considerations needed for future development of high-performance, deformable lithium-ion batteries.

2. Materials and Methods

2.1. LTO Anode Preparation

The spinning suspension of the LTO anode was prepared by mixing carbon-coated LTO powder (LifePower C-T2, SUD-CHEMIE Clariant) with conductive additives, specifically carbon black (Super C65, C-Nergy, Imerys) and carboxyl-functionalized MWCNTs

(US research nanomaterials, Inc.) in a solvent mixture of 4:1 (*v/v*) chloroform: N,N-dimethylformamide (DMF), followed by ultrasonication. Subsequently, Triton X-100 and Poly (ethylene oxide) (PEO) with an average molecular mass of 8 MDa (Sigma-Aldrich) were added to the mixture. The suspension was stirred for at least 24 h to achieve a uniform dispersion of the particles. To optimize the anode suspension formulation, various conditions, combinations of binders, solid loads, and surface-active agents were tested.

To fabricate the anode fibers, the prepared suspension was dispensed through a 25-gauge stainless-steel spinneret at a flow rate of 0.85 mL/h under an applied voltage of 3.5 kV between the needle and the collector. The needle-to-collector distance was 7 cm. The nanofibers were deposited onto copper foil mounted on a rotating grounded drum, resulting in porous electrode meshes. The copper substrate was later utilized as a current collector for the electrochemical characterization of the electrospun anode. To enhance the alignment and uniformity of the fibers, the drum was positioned horizontally on a moving X-stage, which facilitated back-and-forth motion during deposition. All experiments were conducted at room temperature under ambient conditions, with relative humidity maintained between 40% and 50%. The resulting electrospun meshes were vacuum-dried for 12 h to ensure complete solvent evaporation and subsequently were used for the assembly of lithium-ion coin cells.

2.2. Electrochemical Characterization of Electrospun LTO Anode

To evaluate the performance of the electrospun mats, CR2032 coin cell batteries were assembled and tested. The electrospun mat was punched into 12 mm diameter discs, which were then dried overnight at 60 °C under vacuum. The dried electrode discs were subsequently transferred to a glovebox filled with ultra-high-purity argon (content of O_2 and H_2O < 0.1 ppm). Coin cells were assembled using a single sheet of 19 mm diameter commercial polypropylene Celgard 2400 membrane as the separator and a 15 mm diameter Li metal counter electrode. A liquid electrolyte consisting of 0.3 M LiTFSI in $PYR_{14}TFSI$ ionic liquid (IL) electrolyte was used. To examine the reproducibility, at least three coin-cells were assembled and tested for each electrode. Galvanostatic charge/discharge cycling was performed at 30 °C within a voltage window of 1.2–2 V at rates ranging from 0.06 C to 1 C, using a BioLogic BSC-800 battery cycler, Seyssinet-Pariset, France.

Electrochemical impedance spectroscopy (EIS) measurements were performed using a BioLogic VMP3 potentiostat, at the cell's open circuit voltage (OCV) state. The measurements were conducted over a frequency range of 10 kHz to 10 mHz using a 15 mV amplitude.

Cyclic voltammetry (CV) was conducted in a half-cell configuration to assess the performance of the electrospun LTO anode using an ionic liquid electrolyte. Measurements were carried out at a scan rate of 0.1 mVs^{-1}, within the potential window of 1.0–3.0 V (vs. Li^+/Li) at 30 °C.

2.3. Structural Characterization

The morphology of electrospun LTO composite fibers was analyzed using a high-resolution scanning electron microscope (HRSEM, Zeiss Gemini SEM 300, Oberkochen, Germany), equipped with an Energy-Dispersive X-ray Spectroscopy (EDS) detector (X-Flash 6/60, Bruker, Berlin, Germany), operating at an acceleration voltage of 2–5 kV. Additionally, a focused ion beam (FIB) integrated with an HRSEM (Helios 5 UC, ThermoFisher) and EDS detector was employed. A gallium ion FIB probe was used to mill the electrospun LTO electrode fibers and analyze their cross-sectional morphology.

To determine the active material loading in the electrospun fibers, thermogravimetric analysis (TGA) measurements of pristine LTO, PEO (8 MDa), MWCNT, C65 and electrospun

LTO fiber-meshes were performed. Each sample was loaded into an alumina crucible and heated under a dry purified air atmosphere to 800 °C at a rate of 20 °C min^{-1}.

3. Results and Discussion

3.1. Morphology Characterization of Electrospun LTO Anode

The flexible LTO anode was fabricated via a single-step electrospinning process, in which LTO particles were directly incorporated into a spinning suspension with a PEO polymeric binder and conductive additives comprising carbon black (C65) and MWCNTs in a solvent mixture of 4:1 (v/v) CHCl$_3$: DMF. The suspension was electrospun directly onto a copper current collector, forming a fibrous mat without the need for any post-thermal treatment. Eliminating this step allowed preserving the intrinsic flexibility of the as-spun network and avoiding thermal shrinkage and embrittlement typically observed in calcined fibers.

A schematic illustration of the fabrication process and the resulting fibrous LTO mat is shown in Figure 1.
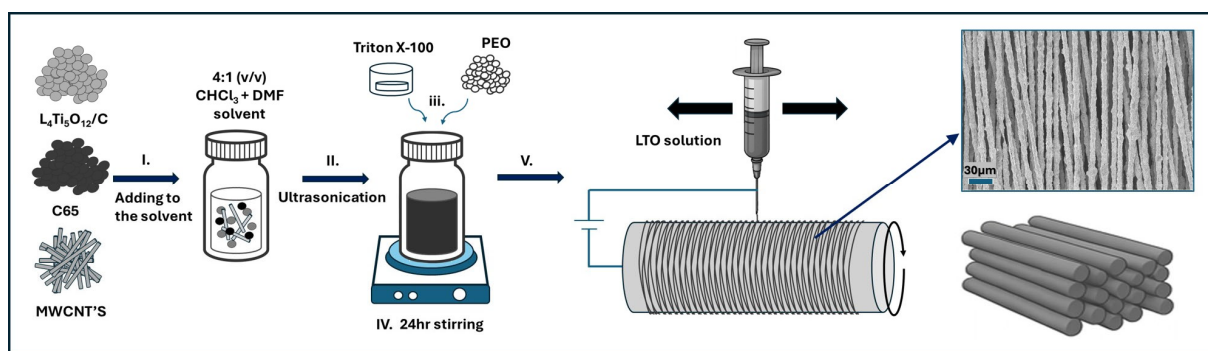

Figure 1. Schematic illustration of the LTO solution preparation process and subsequent fiber formation via electrospinning. The mixture includes L$_4$Ti$_5$O$_{12}$, carbon black (C65), multiwalled carbon nanotubes (MWCNTs), and PEO, dispersed in a CHCl$_3$/DMF solvent system with Triton X-100 as a surfactant. The homogenized ink is electrospun through a syringe to fabricate an aligned fibrous mat.

To establish a reproducible one-step electrospinning of flexible LTO anodes, the suspension formulation and electrospinning parameters were systematically optimized. The goal was to maximize active material loading while ensuring a spinnable suspension that produces continuous, defect-free fibers with minimal bead formation and no mechanical breakage during processing. Controlling bead formation was crucial, as the presence of beads compromises fiber uniformity and disrupts the continuity of the conductive network within the electrode, thereby reducing its effective conductivity [33].

To ensure adequate electrical pathways within the fibrous network, C65 and MWCNTs were co-incorporated into the electrospinning solution. MWCNTs, owing to their high conductivity and large aspect ratio, enable the formation of a percolating conductive network at low loadings (typically below 1.0 wt%), while preserving the flexibility of the fibers [34–36]. PEO was selected as the polymeric binder due to its ability to form flexible, continuous fibers, its proven compatibility with a range of electrode materials, including LTO, and its widespread use in lithium battery systems [37,38], enabling the direct fabrication of mechanically robust electrodes without post-thermal treatment.

Following iterative optimization, the final suspension composition comprised 73 wt% LTO, 14 wt% PEO (8 MDa), 5 wt% C65 (CB) and 7 wt% MWCNT, with 1 wt% Triton-X surfactant to promote uniform dispersion of carbonaceous additives and prevent agglomeration [39]. This formulation yielded uniform, stable fibers with high active material loading

and structural integrity, enabling their direct integration into deformable lithium-ion batteries without additional processing. Figure 2 presents a photograph of the free-standing LTO electrode, detached from the copper substrate for mechanical testing. The electrode maintains its structural integrity under various deformations, including bending, twisting, rolling, and folding, highlighting its excellent mechanical robustness.
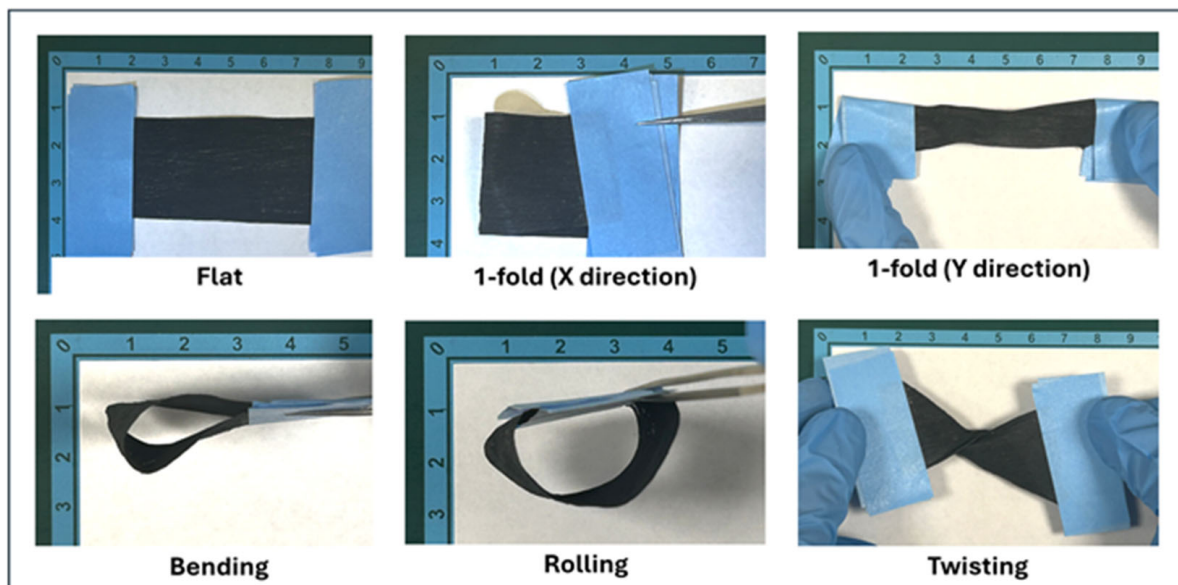

Figure 2. Photos of the resulting LTO fibrous mat under various mechanical deformations: flat, 1-fold (x direction), 1-fold (y direction), bending, rolling, and twisting, demonstrating its high flexibility.

With the optimized formulation and electrospinning parameters established, the resulting fibrous LTO mats were examined using SEM and TGA to evaluate fiber uniformity, active material distribution, and polymer content, as well as to verify that the one-step process yields structurally intact electrodes.

TGA (Figure 3) was performed on both the pristine components and the composite LTO fiber mat to determine active material loading. The profiles of the materials and their derivatives revealed that PEO undergoes complete decomposition at 450 °C, while C65 and MWCTs exhibit thermal stability up to 600 and 700 °C, respectively (Figure 3a), consistent with data reported in the literature [40–42]. Pristine carbon-coated LTO/C (Figure 3b) shows minimal weight loss across a wide temperature range, confirming its high thermal stability. Minor weight losses between 200–300 °C and 350–500 °C are attributed to carbon burn-off in ambient air, with a total carbon content of 1.97 wt% [43,44].

The TGA profile and its derivative for the electrospun LTO fibers (Figure 3a) display two major weight loss regions. The first occurred between 200 °C and 375 °C, corresponding to the decomposition of the polymeric binder. The second, (500–650 °C), is associated with the decomposition of carbon additives (MWCNT and C65) at lower temperatures than the pristine carbon additives. Based on the residual mass, the LTO loading in the electrospun fibers was calculated to be 72 wt%, which closely aligns with the LTO content in the initial jetting suspension mixture.

SEM examination (Figure 4) uncovered the morphological characteristics of the electrospun fibers. High-resolution SEM micrographs (Figure 4a) showed elongated, continuous, and bead-free fibers with an average diameter of 10.03 ± 1.21 μm, forming a porous, interconnected network that is expected to facilitate electrolyte infiltration and lithium-ion transport. To examine internal structure, a FIB was used to section the fibers, with a protective tungsten layer deposited before milling. Cross-sectional SEM micrographs (Figure 4b.i)

revealed that LTO particles were uniformly embedded within a matrix of the polymer binder and the conductive additives.

Elemental mapping (Figure 4b.ii–v) confirmed the homogeneous distribution of titanium (Ti) and oxygen (O), indicative of LTO particles, alongside carbon-rich (C) regions corresponding to the presence of CB particles and MWCNTs. This intimate integration is expected to form a continuous conductive network, providing efficient electron pathways between the current collector and the LTO active material during electrochemical cycling.
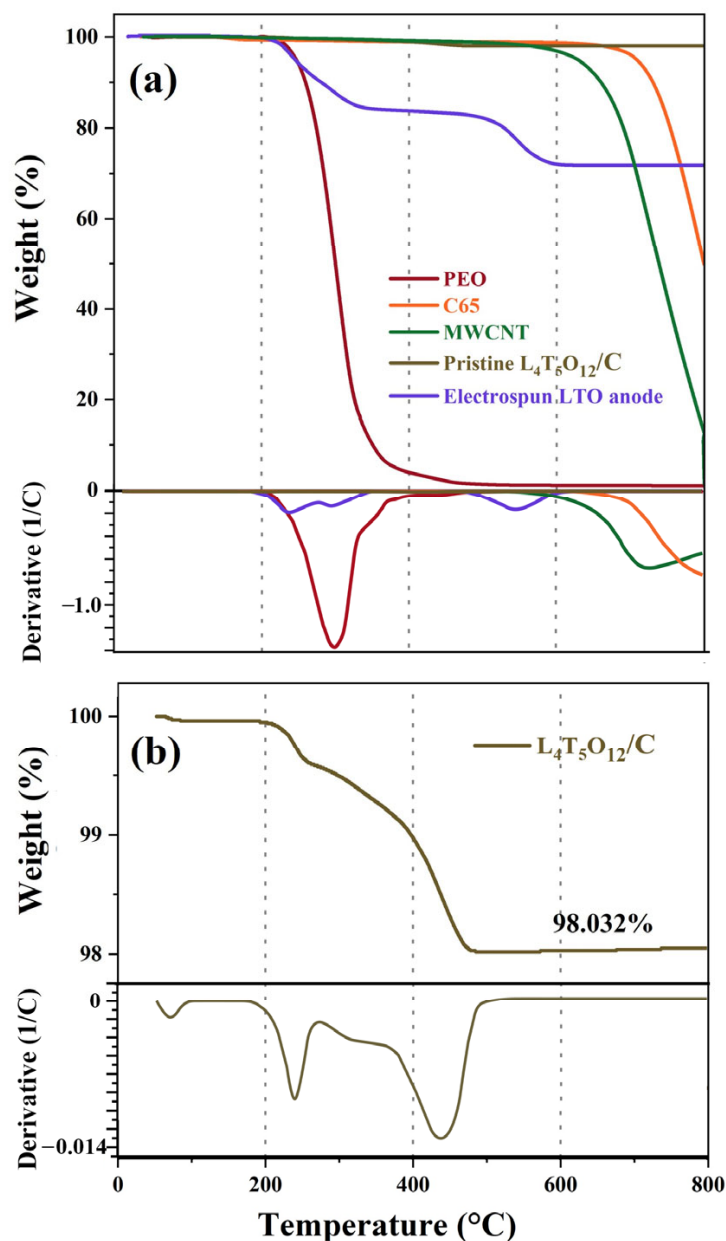

Figure 3. (**a**) TGA plots (top) and derivative (bottom) of the electrospun LTO fibers and their pristine components: PEO, C65, MWCNT and pristine LTO, showing their thermal decomposition behavior up to 800 °C. (**b**) Zoom-in on the TGA curve (top) and derivative (bottom) of pristine LTO, highlighting its weight loss characteristics.
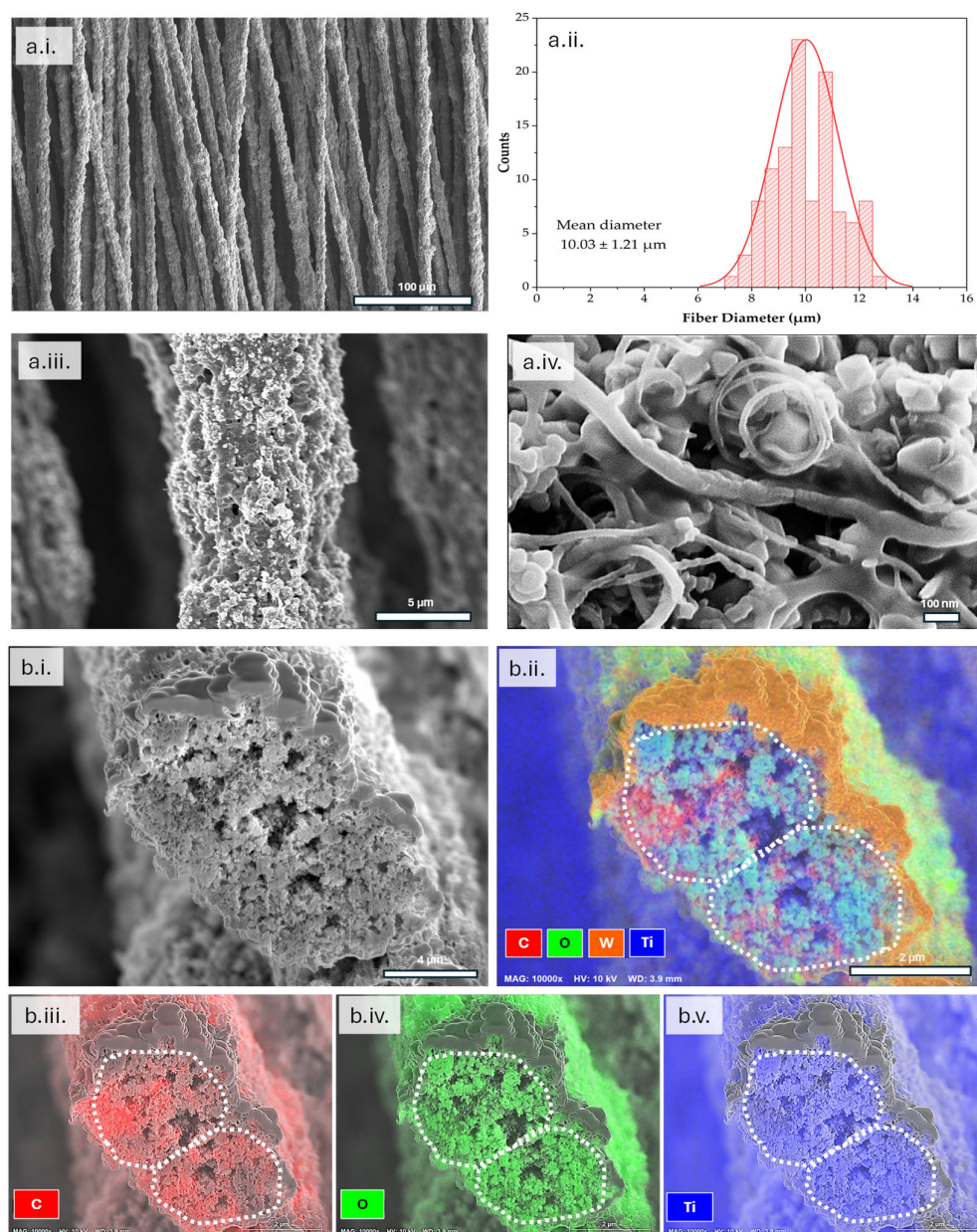
Figure 4. Morphological and elemental characterization of the electrospun LTO fibers. (**a.i**) SEM micrograph showing uniform fibrous architecture. (**a.ii**) Fiber diameter distribution (**a.iii**) SEM micrograph of a single fiber surface (**a.iv**) nanoscale view highlighting the porous texture and the particles distribution (**b**) Fiber's cross-section obtained using the FIB: (i) HRSEM micrograph displaying the internal morphology. (ii) EDS elemental mapping overlay highlighting the distribution of C (red), O (green), and Ti (blue), with white dotted outlines marking two distinct fibers, and W (orange) indicating the residual tungsten protective layer. Individual element maps for (iii) C, (iv) O, and (v) Ti, demonstrating the spatial distribution of key elements within the fibers.

3.2. Electrochemical Characterization

Figure 5 presents the CV profile of the electrospun LTO anode, recorded at a scan rate of 0.1 m Vs^{-1} within the potential range of 1.0–3.0 V (vs Li^+/Li), using 70 μL of $PYR_{14}TFSI$ ionic liquid containing 0.3 M LiTFSI. The electrospun electrode exhibits two distinct redox peaks at 1.39 V and 1.75 V, corresponding to the lithiation and delithiation of the spinel LTO phase, respectively [45]. To maintain the electrode integrity, ionic liquid (IL) $PYR_{14}TFSI$ was used instead of conventional alkyl carbonate electrolytes, since the PEO binder dissolves in carbonate media [46].
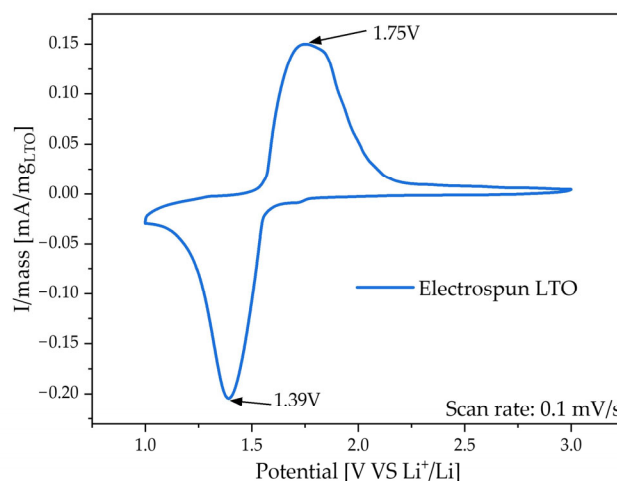
Figure 5. CV profiles of the electrospun LTO electrode measured in a half-cell configuration at a scan rate of 0.1 m Vs^{-1} within the potential range of 1.0–3.0 V (vs. Li$^+$/Li).

Although ILs are often limited by high viscosity and a low Li$^+$ transference number [47,48], they are highly compatible with PEO. Their weak interaction with the polymer prevents binder dissolution while simultaneously enabling Li$^+$ coordination through the ether oxygens in PEO chains [49–51]. Combined with the porous morphology of the spun electrode, these synergistic effects promote local ionic conductivity and Li$^+$ accessibility, resulting in sharper and more distinct redox peaks.

The electrochemical performance of the electrospun LTO fibers was evaluated in a Li half-cell configuration at room temperature, to assess their rate capability and cycling stability. The electrodes had an average active material loading of 1.26 mg LTO·cm^{-2} and were cycled between 1.2 and 2.0 V at identical charge/discharge rates, with current densities ranging from 0.06 to 1 C. Figure 6a presents the galvanostatic charge–discharge profiles at varying C-rates. At 0.06 C the profile displayed a discharge plateau at 1.547 V and a charge plateau at 1.583 V. These reactions involve the reduction of three Ti^{4+} ions to Ti^{3+} during the two-phase transition from spinel-LTO to rock-salt LTO, as described by the following reduction equation [13,52,53]:

$$Li_4Ti_5O_{12} + 3Li^+ + 3e^- \leftrightarrow Li_7Ti_5O_{12} \tag{1}$$
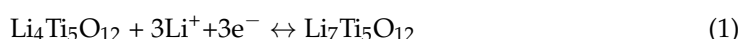
The small polarization at low rate (ΔV = 15.7 mV) (Figure 6a, b) indicates efficient Li$^+$ insertion/extraction pathways within the fibrous network, despite the absence of high-temperature post-treatment. Increasing the current density led to a progressive widening of the voltage gap to 25.3 mV (0.13 C), 117.5 mV (0.68 C), and 202.2 mV (1 C), reflecting growing kinetic limitations associated with restricted Li$^+$ mobility at elevated rates. At higher rates, rapid Li$^+$ consumption at the LTO surface, combined with limited ionic transport in the IL electrolyte, results in pronounced concentration polarization [18,47,48,54]. This leads to localized Li$^+$ depletion (during discharge) or accumulation (during charge), leading to an increase in overpotential. Furthermore, the reformation of the electronically insulating Li$_4$Ti$_5$O$_{12}$ phase during charge exacerbates overpotential under high current conditions [17].

Rate capability results (Figure 6c) show that at low rates, the untreated LTO fibers deliver a discharge capacity of 170 mAh g^{-1}, corresponding to 97% of the theoretical capacity value of spinel LTO (175 mAh g^{-1}). This value surpasses the typical capacities reported in the literature (~160 mAh g^{-1}) [55,56], demonstrating that the electrospun microstructure supports near-complete lithiation at these rates. The electrodes exhibit excellent capacity retention up to 0.13 C, but the performance gradually declines at 0.68 C

(129 mAh g^{-1}) and 1 C (77 mAh g^{-1}), where both ionic transport through the high-viscosity Pyr$_{14}$TFSI-based electrolytes and solid-state Li$^+$ diffusion in LTO are expected to be a limiting factor [18,48,57,58]. Upon returning to 0.13 C, the capacity recovered 95% of its initial value, confirming that the observed limitations are kinetic rather than structural, a key outcome for mechanically robust electrodes. The coulombic efficiency remained near 100% across all rates, with minor deviations at 1 C, attributed to electrolyte transport limitations and surface Li$^+$ depletion at elevated current densities.
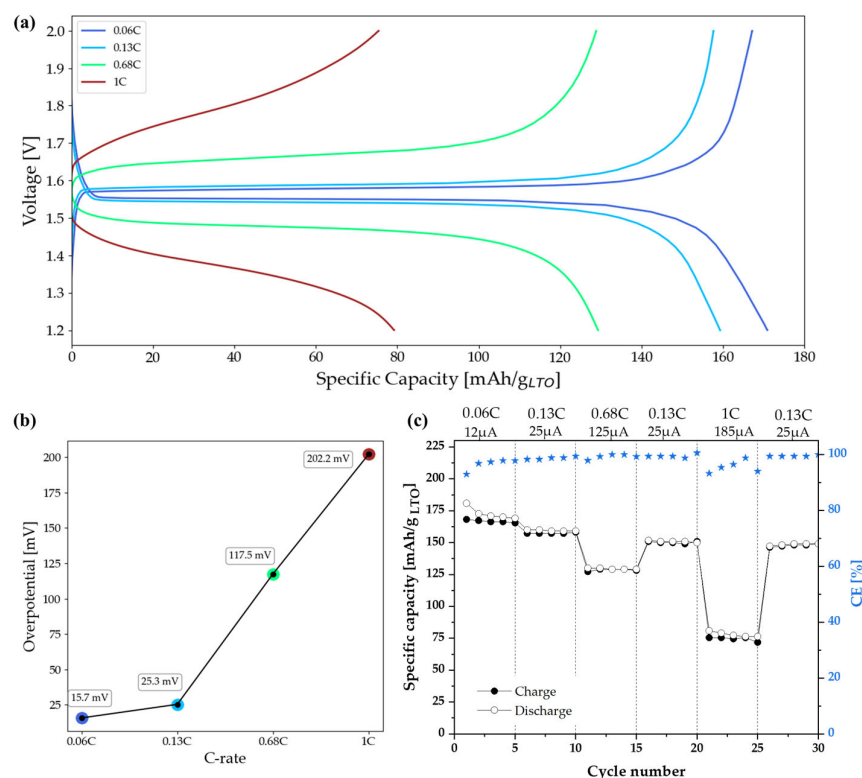

Figure 6. Electrochemical performance of electrospun LTO cells. (**a**) Voltage-specific capacity profiles at different C-rates, illustrating rate-dependent electrochemical behavior (**b**) Overpotential evolution as a function of the C-rate (**c**) Galvanostatic charge–discharge cycling at different current densities with coulombic efficiency (CE) shown as blue stars.

Cycling stability at 0.1 C (Figure 7a) demonstrated stable and high long-term performance, with 160 mAh g^{-1} retained after 200 cycles, corresponding to a negligible capacity loss of 0.01% per cycle and total capacity loss of 1.83%. The coulombic efficiency consistently remained close to 99.6%. This stability reflects both the intrinsic zero-strain property of LTO and the structural cohesion of the electrospun network, which remained intact. EIS measurements were performed at selected stages during the long-term cycling (Figure 7c). Measurements were first conducted after 5 cycles and then after 155 cycles to evaluate stability over extended operation. Beyond this point, EIS was recorded every 20 cycles. All spectra were collected after discharge, following a one-hour rest period to ensure relaxation.

The Nyquist plot (Figure 7c) and the corresponding fitting parameters (Table 1) reveal a dispersion factor (α_d) consistently above 0.65, indicating that the low-frequency region cannot be accurately fitted using a conventional Warburg element. A classical Warburg response typically exhibits a slope of $\pi/4$ and a dispersion parameter of $\alpha_{d=}$ 0.5, whereas the intermediate slopes detected here suggest a mixed reaction between a semi-infinite Warburg element and a finite-space Warburg (FSW) response, generally associated with porous electrode structure and limited ion diffusion [59,60]. To more accurately capture this non-ideal diffusion, a modified restricted diffusion element (Ma) was incorporated

into the equivalent circuit model (Figure 7c, inset). This element, composed of a resistive component (Rd) in parallel with a constant phase element (Qd), accounts for geometry-limited, frequency-dependent diffusion and reproduces the depressed semicircle observed in the spectra. A detailed mathematical description of this model is provided in the Supplementary Materials (S2) [59–63].
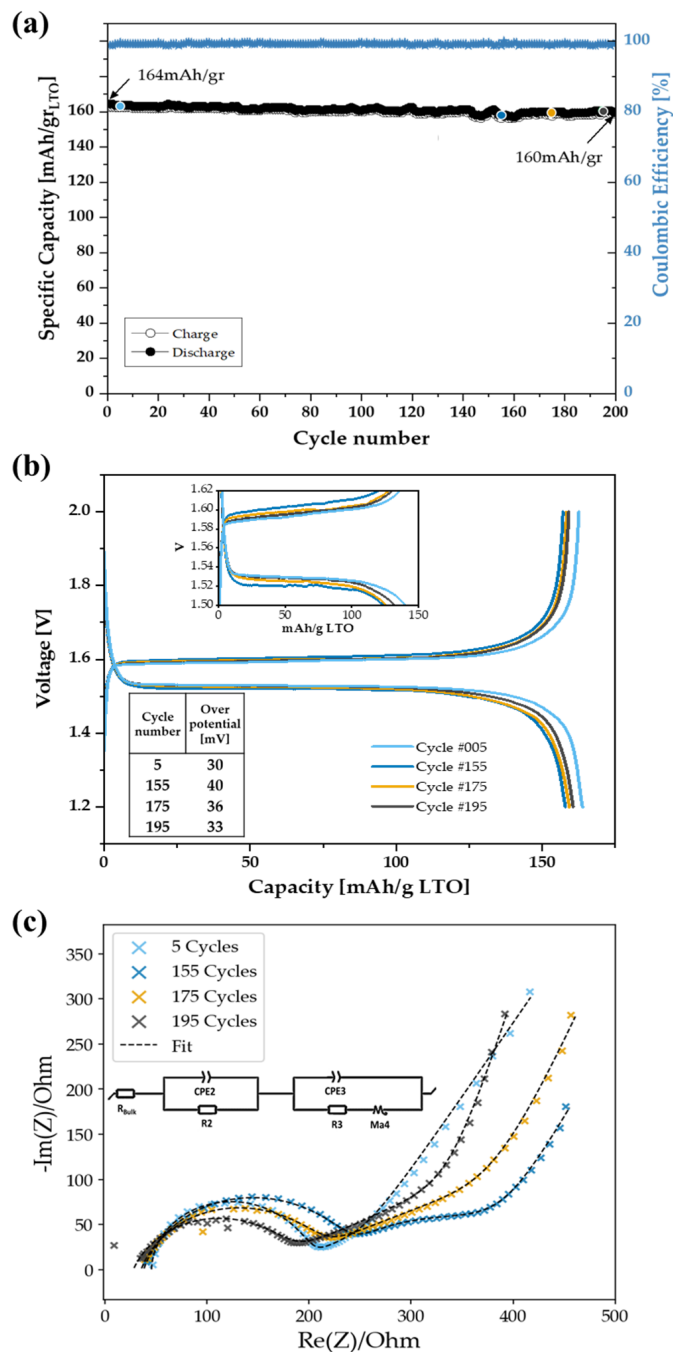

Figure 7. Electrochemical performance of the electrospun LTO anode during cycle life test. (**a**) Long-term cycling stability at 0.1 C, over 200 cycles. (**b**) Charge–discharge profiles at different cycle numbers (5, 155, 175, and 195), highlighting minimal polarization and excellent voltage stability (inset: enlarged plateau region and table of overpotential values). (**c**) Nyquist plots obtained after selected cycles, fitted with the equivalent circuit model (inset), illustrating the evolution of interfacial resistance during cycling.

Table 1. Fitted impedance parameters of the electrospun LTO/Li cell at selected cycle numbers during cycling at 0.1 C. R_{bulk}, R_2, and R_3 are normalized to the geometrical area of the working electrode.

Cycle	R_{bulk} [Ω]	R_2 [Ω]	Q_2 [$\Omega^{-1} \cdot s^\alpha$]	R_3 [Ω]	Q_3 [$\Omega^{-1} \cdot s^\alpha$]	α_d
5	46	133	5.76×10^{-6}	49	5.0×10^{-3}	0.65
155	38	206	1.3×10^{-5}	83.6	9.79×10^{-4}	0.72
175	35	180	1.56×10^{-5}	83.8	1.00×10^{-3}	0.77
195	28	158	1.85×10^{-5}	71.5	1.35×10^{-3}	0.84

Analysis of the impedance evolution highlights distinct trends during cycling. After 5 cycles, the cell exhibited low interfacial resistances and a moderate overpotential (30 mV, Figure 7b), reflecting efficient Li^+ transport in the fresh electrode. By 155 cycles, both R_2 and R_3 had increased substantially, accompanied by a rise in overpotential to 40 mV, indicating the development of interfacial polarization and lower Li transport. While the mid-frequency arc ($R_2 || Q_2$) is often attributed to the active electrode, in a two-electrode configuration it also reflects contributions from the Li electrode, where continuous plating/stripping promotes SEI thickening [64–66]. The simultaneous increase of R_2 and R_3 from cycle 5 to 155, together with the increased Q_2 and depressed semicircle ($\alpha_d > 0.7$), supports the formation of a more resistive interphases, originating from both restructuring of the polymer-salt interphase on the electrospun LTO fibers and thickening of the SEI on Li. These interfacial processes jointly contribute to the polarization observed at mid-life cycling. With continued cycling to 175 and 195 cycles, both R_2 and R_3 partially decreased, accompanied by an increase in α_d toward unity. This behavior suggests a stabilization and reorganization of the electrolyte/electrodes interfaces, possibly facilitated by the one-hour rest period before EIS measurements [67]. Concurrently, the decrease in bulk resistance (R_{bulk}), from 46 Ω after 5 cycles to 28 Ω after 195 cycles, indicates enhanced electrolyte penetration and improved electrode-electrolyte contact, which mitigates ohmic drop across the cell. These findings confirm that the dominant impedance evolution arises from dynamic interfacial processes, rather than intrinsic ohmic resistance.

Overall, these results highlight that the untreated electrospun LTO anode can deliver near-theoretical capacity at low-to-moderate rates, while maintaining stable cycling at moderate current densities. At high rates, performance is primarily constrained by Li^+ transport kinetics rather than structural degradation, with the fibrous architecture and mechanical integrity remaining intact, features essential for flexible battery applications. This balance between structural flexibility and high-rate capability underscores the need for future designs to optimize the system, enabling improved electrochemical performance without compromising the advantages of the one-step fabrication process.

The PEO in the system serves not only as a mechanical binder but also as an ionic conductor through Li^+ coordination with the ether oxygen sites. However, its partial crystallinity at room temperature is expected to limit chain mobility and can locally impede Li^+ transport. Despite this, the optimized PEO content, together with MWCNT and carbon black additives, establishes continuous ionic and electronic pathways. This synergy enables efficient charge transfer while maintaining the fibrous mat's flexibility and mechanical integrity, as evidenced by stable Coulombic efficiency, low interfacial resistance, and minimal polarization during cycling.

While the obtained areal mass loadings are relatively moderate, there is clear potential for improvement within the current fabrication framework. Increasing the active material loading by extending deposition time or stacking multiple fibrous layers could effectively boost capacity. However, excessive thickness may hinder ion transport and solvent evaporation, leading to structural inhomogeneity. Future efforts will therefore focus on tailoring

fiber-mat density and porosity to enhance areal capacity while preserving both mechanical robustness and electrochemical stability.

4. Conclusions

An advanced flexible LTO anode was successfully fabricated via a one-step electrospinning technique, eliminating the need for high-temperature post-treatment. The incorporation of PEO binder with MWCNT and carbon black additives yielded a mechanically robust fibrous mat, capable of withstanding repeated bending, twisting, rolling, and folding without structural degradation. The fibrous architecture enabled a high specific capacity of 170 mAh g^{-1} at 0.06 C (97% of the theoretical value) and excellent long-term cycling stability, with 98.2% capacity retention and >99% coulombic efficiency after 200 cycles at 0.1 C. These results underscore the potential of electrospinning as a scalable and cost-effective strategy for producing flexible, high-performance anodes for next-generation energy storage systems. Further work will focus on enhancing rate capability through optimization of the fiber composition (reducing binder fraction while preserving electrical conductivity and mechanical stability) and exploring electrolyte-electrode interactions to improve Li$^+$ transport. Importantly, coupling this flexible LTO anode with compatible cathode materials in full-cell configurations represents a critical step toward practical, fully flexible lithium-ion batteries for wearable and portable electronics.

Supplementary Materials: The following supporting information can be downloaded at https://www.mdpi.com/article/10.3390/batteries11110405/s1: (S1) Comparison of electrospun flexible LTO and other anode systems by processing temperature and rate performance. (S2) Detailed low-frequency impedance model equations.

Author Contributions: Conceptualization, E.E.M., D.G. and A.S.; methodology, E.E.M., D.G. and A.S.; formal analysis, E.E.M.; investigation, E.E.M., R.A. and N.K.; writing—original draft preparation, review and editing, E.E.M., D.G. and A.S.; supervision, D.G. and A.S. All authors have read and agreed to the published version of the manuscript.

Data Availability Statement: The original contributions presented in this study are included in the article/Supplementary Materials. Further inquiries can be directed to the corresponding author(s).

Conflicts of Interest: The authors declare no conflicts of interest.

Abbreviations

The following abbreviations are used in this manuscript:

LTO	Lithium Titanate Oxide
PEO	Polyethylene Oxide
MWCNT	Multi-Wall Carbon Nanotube
SEI	Solid Electrolyte Interphase

OCV	Open Circuit Voltage
EIS	Electrochemical Impedance Spectroscopy
(HR)SEM	(High Resolution) Scanning Electron Microscope
CV	Cyclic Voltammetry
EDS	Energy Dispersive X-Ray Spectroscopy
TGA	Thermogravimetric Analysis

References

1. Zhao, Y.; Pohl, O.; Bhatt, A.I.; Collis, G.E.; Mahon, P.J.; Rüther, T.; Hollenkamp, A.F. A Review on Battery Market Trends, Second-Life Reuse, and Recycling. *Sustain. Chem.* **2021**, *2*, 167–205. [CrossRef]

2. Gao, Y.; Pan, Z.; Sun, J.; Liu, Z.; Wang, J. *High-Energy Batteries: Beyond Lithium-Ion and Their Long Road to Commercialisation*; Springer: Singapore, 2022; Volume 14.

3. Fan, X.; Liu, B.; Ding, J.; Deng, Y.; Han, X.; Hu, W.; Zhong, C. Flexible and Wearable Power Sources for Next—Generation Wearable Electronics. *Batter. Supercaps* **2020**, *3*, 1262–1274. [CrossRef]

4. Zhang, Q.; Soham, D.; Lian, Z.; Wan, J. Advances in wearable energy storage and harvesting systems. *Med-X* **2025**, *3*, 3. [CrossRef]

5. Wang, N.; Hou, W.; Chang, Y.; Song, H.; Li, H.; Li, Y.; Han, G. Binder-free hydrogen storage composite Co9S8/rGO: A prospective anode for flexible energy storage device with high energy density. *Electrochim. Acta* **2020**, *354*, 136734. [CrossRef]

6. Wang, J.G.; Jin, D.; Zhou, R.; Li, X.; Liu, X.R.; Shen, C.; Xie, K.; Li, B.; Kang, F.; Wei, B. Highly Flexible Graphene/Mn_3O_4 Nanocomposite Membrane as Advanced Anodes for Li-Ion Batteries. *ACS Nano* **2016**, *10*, 6227–6234. [CrossRef]

7. Hu, L.; Liu, N.; Eskilsson, M.; Zheng, G.; McDonough, J.; Wågberg, L.; Cui, Y. Silicon-conductive nanopaper for Li-ion batteries. *Nano Energy* **2013**, *2*, 138–145. [CrossRef]

8. Wang, X.; Lu, X.; Liu, B.; Chen, D.; Tong, Y.; Shen, G. Flexible energy-storage devices: Design consideration and recent progress. *Adv. Mater.* **2014**, *26*, 4763–4782. [CrossRef]

9. Mados, E.; Atar, I.; Gratz, Y.; Israeli, M.; Kondrova, O.; Fourman, V.; Sherman, D.; Golodnitsky, D.; Sitt, A. Polymer-based LFP cathode/current collector microfiber-meshes with bi- and interlayered architectures for Li-ion battery. *J. Power Sources* **2024**, *603*, 234397. [CrossRef]

10. Opra, D.P.; Gnedenkov, S.V.; Sokolov, A.A.; Minaev, A.N.; Kuryavyi, V.G.; Sinebryukhov, S.L. Facile synthesis of nanostructured transition metal oxides as electrodes for Li-ion batteries. *AIP Conf. Proc.* **2017**, *1874*, 397–402.

11. Kavan, L.; Procházka, J.; Spitler, T.M.; Kalbáč, M.; Zukalová, M.; Drezen, T.; Grätzel, M. Li Insertion into $Li_4Ti_5O_{12}$ (Spinel). *J. Electrochem. Soc.* **2003**, *150*, A1000. [CrossRef]

12. Ronci, F.; Reale, P.; Scrosati, B.; Panero, S.; Rossi Albertini, V.; Perfetti, P.; Di Michiel, M.; Merino, J.M. High-resolution in-situ structural measurements of the $Li_{4/3}Ti_{5/3}O_4$ "zero-strain" insertion material. *J. Phys. Chem. B* **2002**, *106*, 3082–3086. [CrossRef]

13. Ohzuku, T.; Ueda, A.; Yamamoto, N. Zero—Strain Insertion Material of $Li[Li_{1/3}Ti_{5/3}]O_4$ for Rechargeable Lithium Cells. *J. Electrochem. Soc.* **1995**, *142*, 1431–1435. [CrossRef]

14. Yan, H.; Zhang, D.; Qilu; Duo, X.; Sheng, X. A review of spinel lithium titanate ($Li_4Ti_5O_{12}$) as electrode material for advanced energy storage devices. *Ceram. Int.* **2021**, *47*, 5870–5895. [CrossRef]

15. Asenbauer, J.; Eisenmann, T.; Kuenzel, M.; Kazzazi, A.; Chen, Z.; Bresser, D. The success story of graphite as a lithium-ion anode material-fundamentals, remaining challenges, and recent developments including silicon (oxide) composites. *Sustain. Energy Fuels* **2020**, *4*, 5387–5416. [CrossRef]

16. Zaghib, K.; Dontigny, M.; Guerfi, A.; Charest, P.; Rodrigues, I.; Mauger, A.; Julien, C.M. Safe and fast-charging Li-ion battery with long shelf life for power applications. *J. Power Sources* **2011**, *196*, 3949–3954. [CrossRef]

17. Wu, K.; Yang, J.; Qiu, X.Y.; Xu, J.M.; Zhang, Q.Q.; Jin, J.; Zhuang, Q.C. Study of spinel $Li_4Ti_5O_{12}$ electrode reaction mechanism byelectrochemical impedance spectroscopy. *Electrochim. Acta* **2013**, *108*, 841–851. [CrossRef]

18. Vasileiadis, A.; de Klerk, N.J.J.; Smith, R.B.; Ganapathy, S.; Harks, P.P.R.M.L.; Bazant, M.Z.; Wagemaker, M. Toward Optimal Performance and In-Depth Understanding of Spinel $Li_4Ti_5O_{12}$ Electrodes through Phase Field Modeling. *Adv. Funct. Mater.* **2018**, *28*, 1705992. [CrossRef]

19. Park, S.K.; Copic, D.; Zhao, T.Z.; Rutkowska, A.; Wen, B.; Sanders, K.; He, R.; Kim, H.K.; De Volder, M. 3D Porous Cu-Composites for Stable Li-Metal Battery Anodes. *ACS Nano* **2023**, *17*, 14658–14666. [CrossRef]

20. Patnaik, S.G.; Jadon, A.; Tran, C.C.H.; Estève, A.; Guay, D.; Pech, D. High Areal Capacity Porous Sn-Au Alloys with Long Cycle Life for Li-ion Microbatteries. *Sci. Rep.* **2020**, *10*, 10405. [CrossRef]

21. Hu, L.; La Mantia, F.; Wu, H.; Xie, X.; McDonough, J.; Pasta, M.; Cui, Y. Lithium-ion textile batteries with large areal mass loading. *Adv. Energy Mater.* **2011**, *1*, 1012–1017. [CrossRef]

22. Wang, A. Three-Dimensional Hierarchical Porous Electrode Structure for Improved Performance in Battery Applications. *Int. J. High Sch. Res.* **2022**, *4*, 1–5. [CrossRef]

23. Lu, H.W.; Zeng, W.; Li, Y.S.; Fu, Z.W. Fabrication and electrochemical properties of three-dimensional net architectures of anatase TiO$_2$ and spinel Li$_4$Ti$_5$O$_{12}$ nanofibers. *J. Power Sources* **2007**, *164*, 874–879. [CrossRef]

24. Xu, H.; Hu, X.; Luo, W.; Sun, Y.; Yang, Z.; Hu, C.; Huang, Y. Electrospun Conformal Li4Ti5O12/C Fibers for High-Rate Lithium-Ion Batteries. *ChemElectroChem* **2014**, *1*, 611–616. [CrossRef]

25. Zhu, N.; Liu, W.; Xue, M.; Xie, Z.; Zhao, D.; Zhang, M.; Chen, J.; Cao, T. Graphene as a conductive additive to enhance the high-rate capabilities of electrospun Li$_4$Ti$_5$O$_{12}$ for lithium-ion batteries. *Electrochim. Acta* **2010**, *55*, 5813–5818. [CrossRef]

26. Sandhya, C.P.; John, B.; Gouri, C. Synthesis and electrochemical characterisation of electrospun lithium titanate ultrafine fibres. *J. Mater. Sci.* **2013**, *48*, 5827–5832. [CrossRef]

27. Abureden, S.; Hassan, F.M.; Lui, G.; Ahn, W.; Sy, S.; Yu, A.; Chen, Z. Multigrain electrospun nickel doped lithium titanate nanofibers with high power lithium ion storage. *J. Mater. Chem. A* **2016**, *4*, 12638–12647. [CrossRef]

28. Zhang, Z.; Deng, X.; Sunarso, J.; Cai, R.; Chu, S.; Miao, J.; Zhou, W.; Shao, Z. Two-Step Fabrication of Li$_4$Ti$_5$O$_{12}$-Coated Carbon Nanofibers as a Flexible Film Electrode for High-Power Lithium-Ion Batteries. *ChemElectroChem* **2017**, *4*, 2286–2292. [CrossRef]

29. Ji, L.; Zhang, X. Electrospun carbon nanofibers containing silicon particles as an energy-storage medium. *Carbon* **2009**, *47*, 3219–3226. [CrossRef]

30. Self, E.C.; McRen, E.C.; Pintauro, P.N. High Performance Particle/Polymer Nanofiber Anodes for Li-ion Batteries using Electrospinning. *ChemSusChem* **2016**, *9*, 208–215. [CrossRef]

31. Self, E.C.; Wycisk, R.; Pintauro, P.N. Electrospun titania-based fibers for high areal capacity Li-ion battery anodes. *J. Power Sources.* **2015**, *282*, 187–193. [CrossRef]

32. Aravindan, V.; Suresh, P.; Sundaramurthy, J.; Ling, W.C.; Ramakrishna, S.; Madhavi, S. Electrospun NiO nanofibers as high performance anode material for Li-ion batteries. *J. Power Sources* **2013**, *227*, 284–290. [CrossRef]

33. Nan, X.; Zhang, Y.; Shen, J.; Liang, R.; Wang, J.; Jia, L.; Yang, X.; Yu, W.; Zhang, Z. A Review of the Establishment of Effective Conductive Pathways of Conductive Polymer Composites and Advances in Electromagnetic Shielding. *Polymers* **2024**, *16*, 2539. [CrossRef]

34. Li, J.; Ma, P.C.; Chow, W.S.; To, C.K.; Tang, B.Z.; Kim, J.K. Correlations between percolation threshold, dispersion state, and aspect ratio of carbon nanotubes. *Adv. Funct. Mater.* **2007**, *17*, 3207–3215. [CrossRef]

35. Burmistrov, I.; Gorshkov, N.; Ilinykh, I.; Muratov, D.; Kolesnikov, E.; Anshin, S.; Mazov, I.; Issi, J.P.; Kusnezov, D. Improvement of carbon black based polymer composite electrical conductivity with additions of MWCNT. *Compos. Sci. Technol.* **2016**, *129*, 79–85. [CrossRef]

36. Ma, P.C.; Liu, M.Y.; Zhang, H.; Wang, S.Q.; Wang, R.; Wang, K.; Wong, Y.K.; Tang, B.Z.; Hong, S.H.; Paik, K.W.; et al. Enhanced electrical conductivity of nanocomposites containing hybrid fillers of carbon nanotubes and carbon black. *ACS Appl. Mater. Interfaces* **2009**, *1*, 1090–1096. [CrossRef]

37. Wen, B.R. Nanostructured Li$_4$Ti$_5$O$_{12}$ as Anode Material for Lithium Ion Batteries. Master's Thesis, Faculty of Science, The University of New South Wales, Kensington, NSW, Australia, 2012.

38. Ragones, H.; Vinegrad, A.; Ardel, G.; Goor, M.; Kamir, Y.; Dorfman, M.M.; Gladkikh, A.; Golodnitsky, D. On the Road to a Multi-Coaxial-Cable Battery: Development of a Novel 3D-Printed Composite Solid Electrolyte. *J. Electrochem. Soc.* **2020**, *167*, 070503. [CrossRef]

39. Li, Q.; Church, J.S.; Kafi, A.; Naebe, M.; Fox, B.L. An improved understanding of the dispersion of multi-walled carbon nanotubes in non-aqueous solvents. *J. Nanopart. Res.* **2014**, *16*, 2513. [CrossRef]

40. Singh, N.K.; Verma, M.L.; Minakshi, M. PEO nanocomposite polymer electrolyte for solid state symmetric capacitors. *Bull. Mater. Sci.* **2015**, *38*, 1577–1588. [CrossRef]

41. Freiberg, A.T.S.; Sicklinger, J.; Solchenbach, S.; Gasteiger, H.A. Li$_2$CO$_3$ decomposition in Li-ion batteries induced by the electrochemical oxidation of the electrolyte and of electrolyte impurities. *Electrochim. Acta* **2020**, *346*, 136271. [CrossRef]

42. Mahajan, A.; Kingon, A.; Kukovecz, Á.; Konya, Z.; Vilarinho, P.M. Studies on the thermal decomposition of multiwall carbon nanotubes under different atmospheres. *Mater. Lett.* **2013**, *90*, 165–168. [CrossRef]

43. Zhu, G.-N.; Wang, C.-X.; Xia, Y.-Y. A Comprehensive Study of Effects of Carbon Coating on Li$_4$Ti$_5$O$_{12}$ Anode Material for Lithium-Ion Batteries. *J. Electrochem. Soc.* **2011**, *158*, A102. [CrossRef]

44. Yuan, T.; Yu, X.; Cai, R.; Zhou, Y.; Shao, Z. Synthesis of pristine and carbon-coated Li$_4$Ti$_5$O$_{12}$ and their low-temperature electrochemical performance. *J. Power Sources* **2010**, *195*, 4997–5004. [CrossRef]

45. Agrawal, R.; Hao, Y.; Song, Y.; Chen, C.; Wang, C. Hybridization of lithium-ion batteries and electrochemical capacitors: Fabrication and challenges. *Energy Harvest. Storage Mater. Devices Appl. VI* **2015**, *9493*, 94930B.

46. Appetecchi, G.B.; Aihara, Y.; Scrosati, B. Investigation of swelling phenomena in PEO-based polymer electrolytes: II. Chemical and electrochemical characterization. *Solid State Ionics* **2004**, *170*, 63–72. [CrossRef]

47. Montanino, M.; Moreno, M.; Carewska, M.; Maresca, G.; Simonetti, E.; Lo Presti, R.; Alessandrini, F.; Appetecchi, G.B. Mixed organic compound-ionic liquid electrolytes for lithium battery electrolyte systems. *J. Power Sources* **2014**, *269*, 608–615. [CrossRef]

48. Castiglione, F.; Ragg, E.; Mele, A.; Appetecchi, G.B.; Montanino, M.; Passerini, S. Molecular environment and enhanced diffusivity of Li+ ions in lithium-salt-doped ionic liquid electrolytes. *J. Phys. Chem. Lett.* **2011**, *2*, 153–157. [CrossRef]

49. Diddens, D.; Heuer, A. Simulation study of the lithium ion transport mechanism in ternary polymer electrolytes: The critical role of the segmental mobility. *J. Phys. Chem. B* **2014**, *118*, 1113–1125. [CrossRef] [PubMed]

50. An, Y.; Han, X.; Liu, Y.; Azhar, A.; Na, J.; Nanjundan, A.K.; Wang, S.; Yu, J.; Yamauchi, Y. Progress in Solid Polymer Electrolytes for Lithium-Ion Batteries and Beyond. *Small* **2022**, *18*, 1–36. [CrossRef]

51. Guchok, O.; Ardel, G.; Keidar, T.D.; Nakar, H.; Ragones, H.; Kaplan, D.; Zheng, A.; Greenbaum, S.; Lounev, I.; Greenbaum, A.; et al. Understanding of the ion transport in blended TPU-PEO polymer electrolytes. *J. Solid State Electrochem.* **2025**. [CrossRef]

52. Zaghib, K.; Simoneau, M.; Armand, M.; Gauthier, M. Electrochemical study of $Li_4Ti_5O_{12}$ as negative electrode for Li-ion polymer rechargeable batteries. *J. Power Sources* **1999**, *81–82*, 300–305. [CrossRef]

53. Sun, X.; Radovanovic, P.V.; Cui, B. Advances in spinel $Li_4Ti_5O_{12}$ anode materials for lithium-ion batteries. *New J. Chem.* **2015**, *39*, 38–63. [CrossRef]

54. Kim, J.H.; Song, S.W.; Van Hoang, H.; Doh, C.H.; Kim, D.W. Study on the cycling performance of Li4Ti5O 12 electrode in the ionic liquid electrolytes containing an additive. *Bull. Korean Chem. Soc.* **2011**, *32*, 105–108. [CrossRef]

55. Huynh, L.T.N.; Ha, C.T.D.; Nguyen, V.D.; Nguyen, D.Q.; Le, M.L.P.; Tran, V.M. Structure and Electrochemical Properties of $Li_4Ti_5O_{12}$ Prepared via Low-Temperature Precipitation. *J. Chem.* **2019**, *2019*, 1727859. [CrossRef]

56. Zaghib, K.; Armand, M.; Gauthier, M. Electrochemistry of Anodes in Solid—State Li—Ion Polymer Batteries. *J. Electrochem. Soc.* **1998**, *145*, 3135–3140. [CrossRef]

57. Elia, G.A.; Ulissi, U.; Jeong, S.; Passerini, S.; Hassoun, J. Exceptional long-life performance of lithium-ion batteries using ionic liquid-based electrolytes. *Energy Environ. Sci.* **2016**, *9*, 3210–3220. [CrossRef]

58. Ara, M.; Meng, T.; Nazri, G.-A.; Salley, S.O.; Simon Ng, K.Y. Ternary Imidazolium-Pyrrolidinium-Based Ionic Liquid Electrolytes for Rechargeable Li-O$_2$ Batteries. *J. Electrochem. Soc.* **2014**, *161*, A1969–A1975. [CrossRef]

59. Diard, J.-P.; Le Gorrec, B.; Montella, C. Diffusion Impedances. In *Handbook of Electrochemical Impedance Spectroscopy*; Electrical Circuits Containing CPEs, Bio-Logic: Seyssinet-Pariset, France, 2013.

60. Cabanel, R.; Barral, G.; Diard, J.P.; Le Gorrec, B.; Montella, C. Determination of the diffusion coefficient of an inserted species by impedance spectroscopy: Application to the H/H$_x$Nb$_2$O$_5$ system. *J. Appl. Electrochem.* **1993**, *23*, 93–97. [CrossRef]

61. Macdonald, J.R. Impedance Spectroscopy. *Ann. Biomed. Eng.* **1992**, *20*, 289–305. [CrossRef] [PubMed]

62. Waluś, S.; Barchasz, C.; Bouchet, R.; Alloin, F. Electrochemical impedance spectroscopy study of lithium–sulfur batteries: Useful technique to reveal the Li/S electrochemical mechanism. *Electrochim. Acta* **2020**, *359*, 136944. [CrossRef]

63. Gateman, S.M.; Gharbi, O.; Gomes de Melo, H.; Ngo, K.; Turmine, M.; Vivier, V. On the use of a constant phase element (CPE) in electrochemistry. *Curr. Opin. Electrochem.* **2022**, *36*, 101133. [CrossRef]

64. Jagger, B.; Pasta, M. Solid electrolyte interphases in lithium metal batteries. *Joule* **2023**, *7*, 2228–2244. [CrossRef]

65. Peled, E. The Electrochemical Behavior of Alkali and Alkaline Earth Metals in Nonaqueous Battery Systems—The Solid Electrolyte Interphase Model. *J. Electrochem. Soc.* **1979**, *126*, 2047–2051. [CrossRef]

66. Perez-Beltran, S.; Kuai, D.; Balbuena, P.B. SEI Formation and Lithium-Ion Electrodeposition Dynamics in Lithium Metal Batteries via First-Principles Kinetic Monte Carlo Modeling. *ACS Energy Lett.* **2024**, *9*, 5268–5278. [CrossRef] [PubMed]

67. Hosen, M.S.; Gopalakrishnan, R.; Kalogiannis, T.; Jaguemont, J.; Van Mierlo, J.; Berecibar, M. Impact of Relaxation Time on Electrochemical Impedance Spectroscopy Characterization of the Most Common Lithium Battery Technologies—Experimental Study and Chemistry-Neutral Modeling. *World Electr. Veh. J.* **2021**, *12*, 77. [CrossRef]